









RESEARCH ARTICLE | MARCH 29 2023

Formation mechanism of trench defects in green InGaN/GaN multiple quantum wells

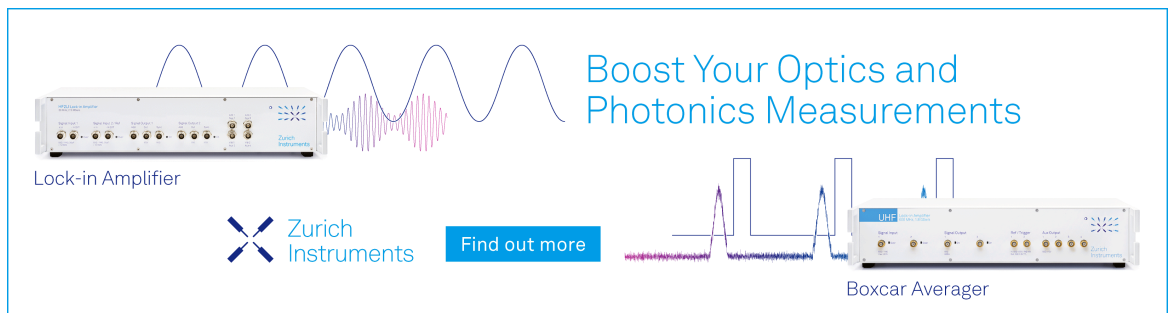
Zhiming Shi ; Aiqin Tian ; Xiaojuan Sun ; Xuan Li ; Hang Zang; Xujun Su; Hao Lin; Peng Xu; Hui Yang; Jianping Liu  ; Dabing Li  



J. Appl. Phys. 133, 123103 (2023)
<https://doi.org/10.1063/5.0136104>



CrossMark



Boost Your Optics and Photonics Measurements

Lock-in Amplifier

Zurich Instruments

Find out more

Boxcar Averager

Formation mechanism of trench defects in green InGaN/GaN multiple quantum wells

Cite as: J. Appl. Phys. 133, 123103 (2023); doi: 10.1063/5.0136104

Submitted: 2 December 2022 · Accepted: 11 March 2023 ·

Published Online: 29 March 2023



Zhiming Shi,¹ Aiqin Tian,^{2,3} Xiaojuan Sun,¹ Xuan Li,^{2,3} Hang Zang,¹ Xujun Su,^{2,3} Hao Lin,^{2,3} Peng Xu,⁴ Hui Yang,² Jianping Liu,^{2,3,4,a)} and Dabing Li^{1,a)}

AFFILIATIONS

¹State Key Laboratory of Luminescence and Applications, Changchun Institute of Optics, Fine Mechanics and Physics, Chinese Academy of Sciences, Changchun 130033, People's Republic of China

²Suzhou Institute of Nano-tech and Nano-bionics, Chinese Academy of Sciences, Suzhou 215123, People's Republic of China

³Key Laboratory of Nanodevices and Applications, Chinese Academy of Sciences, Suzhou 215123, People's Republic of China

⁴Guangdong Institute of Semiconductor Micro-nano Manufacturing Technology, Foshan 528000, People's Republic of China

^{a)}Authors to whom correspondence should be addressed: jpiliu2010@sinano.ac.cn and lidb@ciomp.ac.cn

ABSTRACT

Trench defects, resulting in low emission efficiency in green and longer spectrum ranges, are widely observed in III-nitride alloy multiple quantum wells (MQWs), particularly in those with high indium content. There is a lack of understanding of the atomic formation mechanism of trench defects; however, it is crucial to the efficiency of devices. Here, we provided a thermodynamic analysis through first-principles calculations based on the density functional theory combined with experimental confirmation to reveal the atomic formation mechanism of trench defects in the InGaN MQWs system. The In-rich region is easy to form and induces basal plane stacking faults (BSFs) at the interface between the InGaN quantum well and the GaN quantum barrier (QB). The boundary between BSF and non-BSF regions exhibits a much slower growth rate due to the formation of homoelementary bonds, resulting in a V-shaped groove shape. Based on high-angle annular dark field scanning transmission electron microscopy, we observe the trench defects originating from the thick GaN QB layer due to the formation of closed-loop V-shaped grooves and the BSF. Besides, the cathodoluminescence measurements show that the InGaN QW within the defect has excess indium and poor crystal quality.

14 March 2024 06:43:58

Published under an exclusive license by AIP Publishing. <https://doi.org/10.1063/5.0136104>

I. INTRODUCTION

III-nitride semiconductors are important candidates and have obtained great success for photoelectronic and power electronic applications.^{1–5} However, this system is criticized for the high density of defects, including point defects, dislocations, and trench defects.^{6,7} These defects usually act as nonradiative or current leakage centers to poison the quantum efficiency of devices.^{8,9} The point defects and dislocations were widely observed in all III-nitrides and their multicomponent alloys due to serious strain and the big difference in atomic diffusion barriers^{10,11} and, thus, have attracted the most attention.

The trench defect, a kind of V-shaped groove boundary with a closed-loop, almost exists in the materials with indium components, such as InGaN/GaN multiple quantum wells (MQWs),⁷ InGaN epilayers,¹² and AlInGaN QWs.¹³ It is attributed to the

notorious “green gap.”^{14–16} A clear understanding of the formation mechanism of trench defects is essential to mitigate the defect density and improve the efficiency of optoelectronic devices. Many experimental observations have demonstrated that trench defects are always caused by basal stacking faults (BSFs). Massabuau *et al.* deduced that trench defects in InGaN/GaN QWs may be induced by stacking mismatch boundaries (SMBs) through TEM and atomic force microscopy (AFM) characterization.⁷ Smalc-Koziorowska *et al.* identified the trench defects formed on SMBs in GaN quantum barriers (QBs), and they can be suppressed when the growth temperature is higher than 830 °C.¹⁷ Meanwhile, the efficiency reduction in InGaN/GaN light-emitting diodes (LEDs) induced by trench defects was confirmed by cathodoluminescence.^{18,19} However, the physical understanding of the formation kinetics of trench defects is quite deficient. At present, two questions

remain unclear: (1) What is the relationship between indium segregation and the formation of BSFs? (2) Why are the trench defects more likely to form in GaN QBs than in InGaN QWs?

In this article, we provide a thermodynamic analysis through first-principles calculations based on the density functional theory (DFT) combined with experimental confirmation to reveal the atomic formation mechanism of trench defects in InGaN MQWs. We find that the exposed In-rich surface is more stable than others during growth. The BSFs are easier to form on In-rich surfaces than on Ga-rich surfaces, and the trench defect formed due to the slow growth along SMBs. Our conclusion is confirmed by high-angle annular dark field scanning transmission electron microscopy (HAADF-STEM). The BSFs, which originate at the interface between the InGaN quantum well (QW) and GaN QB, are observed in the GaN QBs. Then, scanning electron microscopy (SEM) and cathodoluminescence (CL) are performed to confirm that the InGaN QW within the trench included indium segregation.

II. THEORETICAL AND EXPERIMENTAL METHODS

A. First-principles calculation methods

All calculations are performed based on density functional theory (DFT) methods as implemented in the VASP package.²⁰ The projector-augmented wave (PAW)²¹ method for the core region and Perdew–Burke–Ernzerhof (PBE) for the exchange–correlation potential of valence electrons are employed.²² A kinetic energy cutoff of 500 eV is chosen for the plane-wave expansion. The DFT-D3 correction is adopted to describe the long-range van der Waals interaction.²³ The wurtzite (WZ) slabs ($2 \times 2 \times 3$ supercell) with the cationic surface are used to investigate the thermodynamic stability of the surface, the bottom N atoms are passivated by hydrogen, and the vacuum is larger than 10 Å to avoid the imaginary interaction between adjacent periods. The atomic configurations are shown in Fig. 1. The bottom four atomic layers stand for GaN QBs, and the top two atomic layers are epilayers. The x in $\text{In}_x\text{Ga}_{1-x}\text{N}$ is in the range of 0–0.50 with a 0.125 interval, which is consistent with that in $\text{In}_x\text{Ga}_{1-x}\text{N}$ green lasers. To mimic different distributions of indium atoms, we considered three surface structures for one indium component: (a) pure GaN surfaces (Surface_Ga), where indium atoms are in the bulk phase; (b) homogenous surfaces (Surface_InGaN), where gallium and indium atoms distribute homogeneously on the surface; and (c) In-rich surfaces, where indium atoms segregate on the surface (Surface_In). The density k -mesh is set to $0.04 2\pi/\text{Å}$ for structural relaxation and to $0.02 2\pi/\text{Å}$ for electronic property calculations. The geometric optimization is performed with the conjugate gradient scheme, and the atomic positions are relaxed until the maximum force on each atom is less than $0.01 \text{ eV}/\text{Å}$. The 5 ps Born–Oppenheimer molecular dynamics (BOMD) simulation is performed by using a $4 \times 4 \times 3$ supercell under the NVT ensemble. The Andersen thermostat and a 1 fs time step are used. The bottom two layers are fixed during structural relaxation and BOMD simulations.

B. Epitaxy and characterization techniques

InGaN/GaN MQW samples with four pairs of InGaN/GaN MQWs capped with a 50 nm GaN layer are grown on a c -plane

sapphire substrate by a low-pressure metal-organic chemical vapor deposition (MOCVD) reactor. Triethyl-gallium (TEGa), trimethyl-indium (TMIn), and ammonia (NH_3) are used as precursors for Ga, In, and N, and N_2 is the carrier gas of InGaN/GaN MQWs. The InGaN QWs and GaN QBs are grown at the same temperature. The MQW samples with different emission wavelengths are obtained by adjusting the growth temperature while keeping the TEGa and TMIn source flows constant to study the influence of indium content on the density of trench defects. The growth temperatures of MQW samples with PL wavelengths of 460, 520, and 566 nm are 740, 710, and 680 °C, respectively. Atomic force microscopy (AFM) in the tapping mode is performed on the Bruker Dimension ICON to evaluate the morphology of all samples with different emission wavelengths. The SEM and CL (SEM&CL) measurements with an accelerating voltage of 3 kV are also performed for the sample with a peak wavelength of 520 nm to investigate the luminescence properties inside and outside the trench defects. The SEM&CL measurements are performed on the Nova NanoSEM450 from Nano-X of Suzhou Institute of Nano-Tech and Nano-Bionics, Chinese Academy of Sciences (SINANO). The HAADF-STEM is performed on FEI Themis Z to analyze the microstructure of the trench defects.

III. RESULTS AND DISCUSSIONS

A. Thermodynamic stability of different surface structures

First, the thermodynamic stabilities of Surface_Ga, Surface_InGaN, and Surface_In, with the indium component of the InGaN epilayers in the range from 0 to 0.50, are taken into consideration. The Surface_In structures have the lowest free energies and the highest thermodynamic stability when comparing total free energies of surface structures, as shown in Fig. 2(a) (black lines). The indium component has an impact on stability. As the x increased in the $\text{In}_x\text{Ga}_{1-x}\text{N}$ epilayer, the energy differences between the Surface_In and Surface_Ga structures, defined as $\Delta E_{\text{surface}} = E_{\text{surface_In}} - E_{\text{surface_Ga}}$, grew from 1.12 eV and finally converged around 2.53 eV at $x \geq 0.375$, as shown in Fig. 2(a) (red line). The sole exception, which will be explained later, is the situation at $x=0.50$ when Surface_InGaN is more stable than Surface_In. The stability of the surface is controlled by the characteristics of chemical bonds because the surface is made up of cationic dangling bonds. The calculated bond energies are 3.69 eV for Ga–N and 2.80 eV for In–N, respectively, indicating that dangling indium atoms exhibit better stability than dangling gallium atoms. Therefore, a surface with more dangling indium atoms is more stable than one with more dangling gallium atoms. It is also confirmed by the projected DOS. The $\text{In}_{0.25}\text{Ga}_{0.75}\text{N}$ is adopted as the example. As shown in Fig. 2(b), the contributions of indium near the Fermi level follow the order of Surface_Ga < Surface_InGaN < Surface_In, while the order of free energy is Surface_In < Surface_InGaN < Surface_Ga. Moreover, the dangling indium atoms that are hanging from the surface can stabilize the dangling gallium atoms, as shown by the partial charge density near the Fermi level in Fig. 2(c). The contributions from dangling gallium atoms are weakened as the indium-content increases. For instance, the Surface_In of $\text{In}_{0.25}\text{Ga}_{0.75}\text{N}$ is made up of four

14 March 2024, 06:43:58

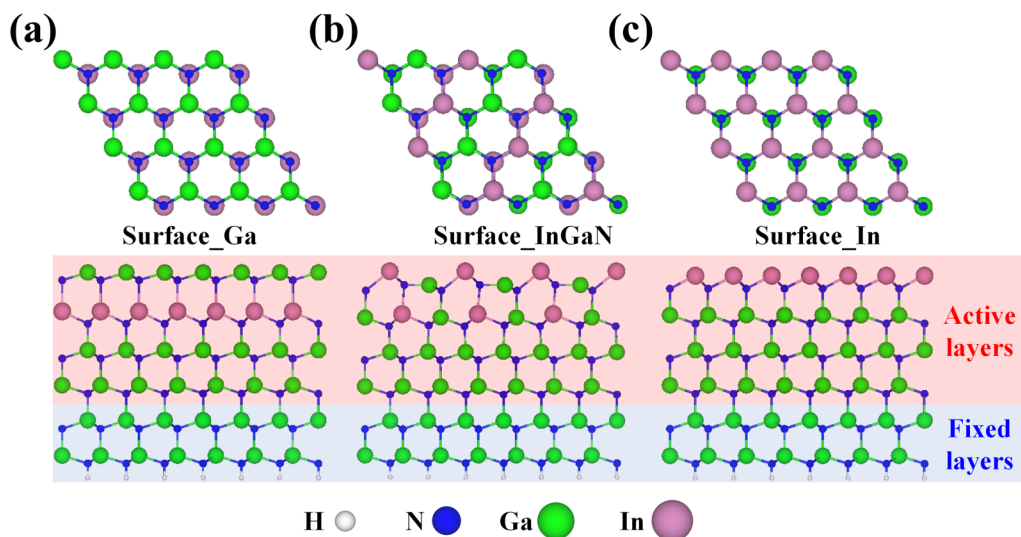


FIG. 1. The top (up) and side (down) views of atomic structures used in first-principles calculations. The (a) Surface_Ga, (b) Surface_InGaN, and (c) Surface_In of $\text{In}_{0.50}\text{Ga}_{0.50}\text{N}$ are adapted as examples. The bottom two layers are fixed during relaxations and BOMD simulations. The white, blue, green, and purple balls represent H, N, Ga, and In atoms, respectively.

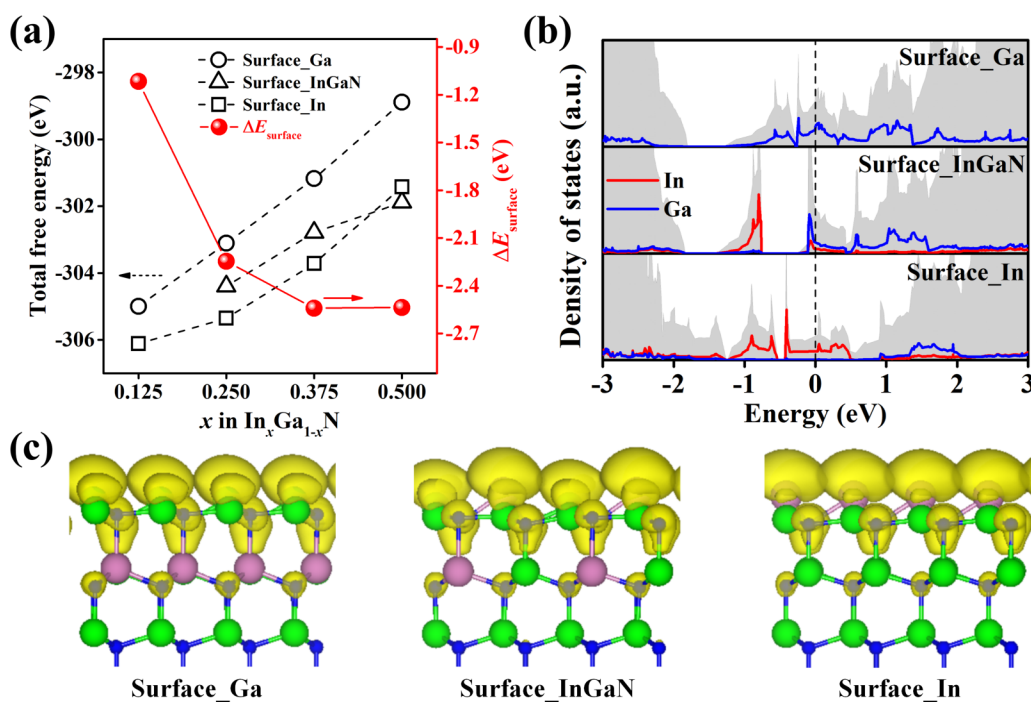


FIG. 2. The stability of different surface structures. (a) The free energy and surface energy difference ($\Delta E_{\text{surface}}$) with the In component. (b) The projected DOS and (c) charge density near the Fermi level for the $\text{In}_{0.25}\text{Ga}_{0.75}\text{N}$ epilayer with different surface structures. The red and blue lines in (b) are the projected DOS for dangling In and Ga bonds, the gray shadow stands for total DOS, and the Fermi level is marked by the black dashed line. The isosurface in (c) is set to $5 \times 10^{-3} \text{ e}/\text{\AA}^3$.

14 March 2024 06:43:58

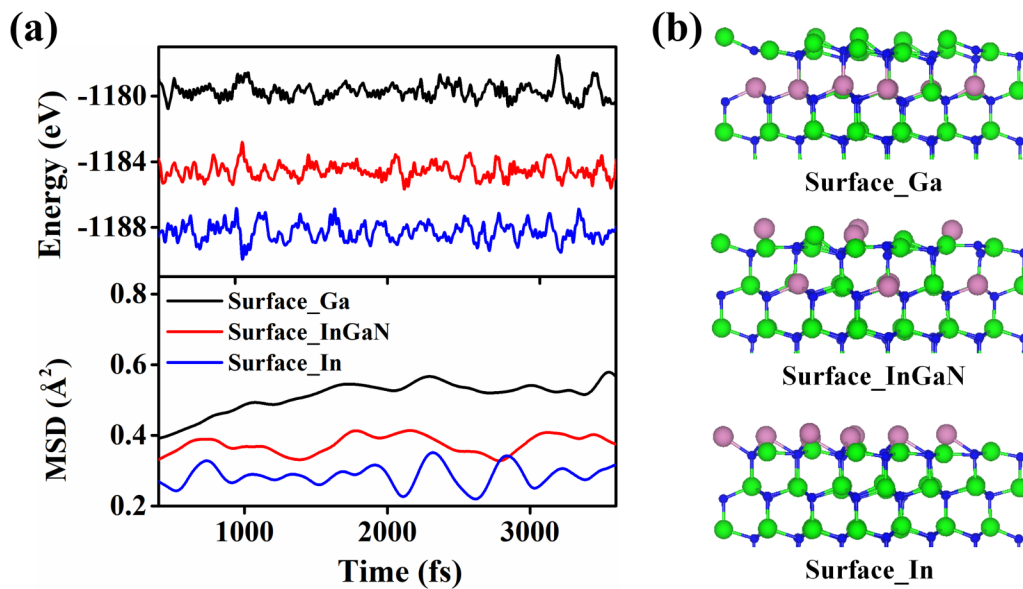


FIG. 3. The results of BOMD simulations for $\text{In}_x\text{Ga}_{1-x}\text{N}$. (a) The total energy evaluation (upper) and the mean-square-deviation (MSD) of the surface cations' atomic position (down) as a function of time for different surfaces. (b) The snapshots of different surface structures at the end of BOMD simulation.

dangling indium and four gallium atoms, but the states at the Fermi level are entirely provided by dangling indium atoms.

We performed BOMD simulations for $\text{In}_{0.25}\text{Ga}_{0.75}\text{N}$ structures to assess the relative kinetic stability of different surface structures. The simulation lasted for a total of 5 ps at 300 K, of which we chose the final 3 ps to study the surface stability. The energies fluctuate around the equilibrium position, as shown in Fig. 3(a). The Surface_In is the most stable configuration among the three considered cases [Fig. 3(a)]. The magnitude of the vibration of dangling bonds is evaluated using the mean-square deviation (MSD). Greater MSD suggests more severe vibration. The results agree with energy fluctuations. As a result, the excellent stability of Surface_In may be the decisive factor in the formation of In-rich segregation regions in InGaN MQWs. The snapshots at the end of BOMD simulations are displayed in Fig. 3(b).

Due to the lattice mismatch between GaN and InGaN, the structures always experience significant strain, which is competitive with the indium component to affect the surface stability. The anomalous spot in Fig. 2(a) at $x=0.50$ may be the result of the strain effect due to the increased lattice mismatch between GaN and InGaN. We collect Surface_InGaN and Surface_In for $\text{In}_{0.50}\text{Ga}_{0.50}\text{N}$ as an example to reveal the relationship between the stability and strain, as shown in Fig. 4. Here, only tensile stress (positive values for strain, from 1% to 5%) is applied since the InGaN epilayers experience the largest compressive stress on GaN QBs at the zero strain point, and the compression gradually releases with increasing strain. The total free energy continuously rises as the strain increases, which is reasonable. Surface_InGaN is more stable than Surface_In when the strain is smaller than 2% because the free energy increase from the strain compensates for the effect of stabilization induced by more dangling indium atoms. It inverses

as the strain is more than 3% due to the release of strain. Therefore, the stability of surface structures can be tuned by strain engineering.

B. The thermodynamic stability of different stacking orders

The thermodynamic stability of various stacking orders is examined, as the BSF is caused by a stacking fault between wurtzite

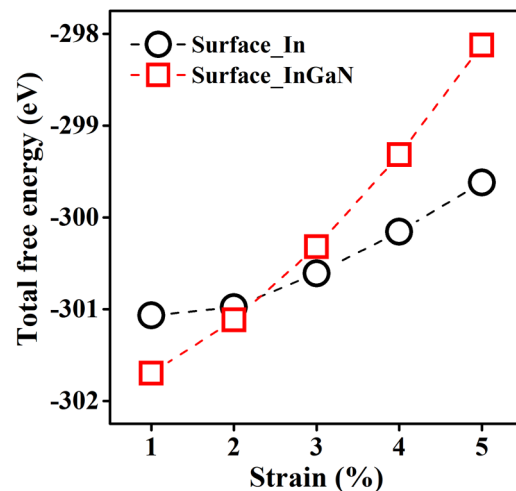


FIG. 4. The total free energy as the function of strain for $\text{In}_{0.50}\text{Ga}_{0.50}\text{N}$.

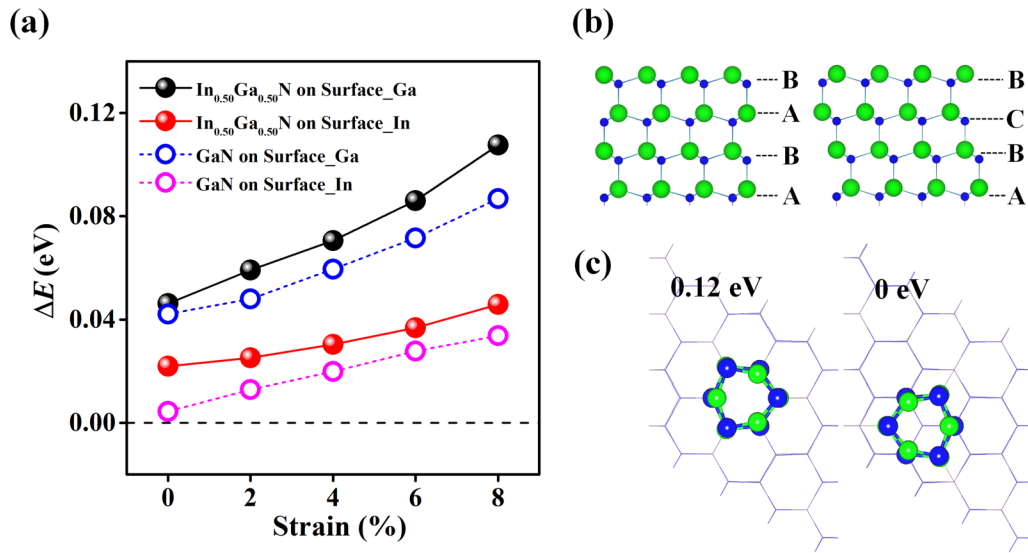


FIG. 5. The stability of different stacking orders. (a) The free energy difference (ΔE) as the function of strain. (b) The atomic configuration of the stacking fault. (c) The stability of GaN cores on Surface_In slab.

(WZ) and zinc blende (ZB) phases (ABAB-stacking for the WZ phase, ABCABC-stacking for the ZB phase). We consider the ABCB-stacking slab and compare its thermodynamic stability to the WZ slab, as shown in Fig. 5(a). Four cases are included, InGaN stacks on Surface_Ga (QB/QW interface); InGaN stacks on Surface_In (growth of InGaN QWs); GaN stacks on Surface_Ga (growth of GaN QBs); and GaN stacks on Surface_In (QW/QB interface). The schemes for stacking orders are displayed in Fig. 5(b). ΔE (define as $\Delta E = E_{\text{ABCB}} - E_{\text{ABAB}}$) is used to estimate the stability for stacking orders. The positive values [in Fig. 5(a)] indicate the poorer stability of ABCB-stacking than that of

ABAB-stacking. It is reasonable due to the better stability of the WZ phase than the ZB phase for III-nitrides. The GaN on the Surface_In system shows the smallest ΔE of 0.004 eV, inferring the comparable thermodynamic stability between ABCB- and ABAB-stacking. The quite small energy difference is ready to be compensated under the growth condition. Since the trench defects originate at QW/QB interfaces and evolve in GaN QB, it follows that the BSF is more likely to occur there than in other locations. Moreover, we compare the calculated adsorption energy of a small GaN core (including 12 atoms) absorbed on Surface_In with different stacking orders. From Fig. 5(c), we can find that

14 March 2024 06:43:58

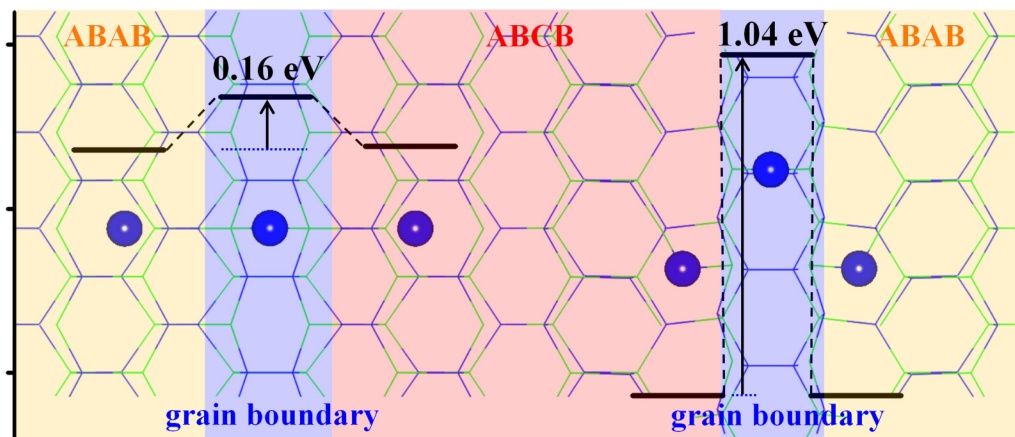


FIG. 6. N adatom binding energy at different positions around a grain boundary.

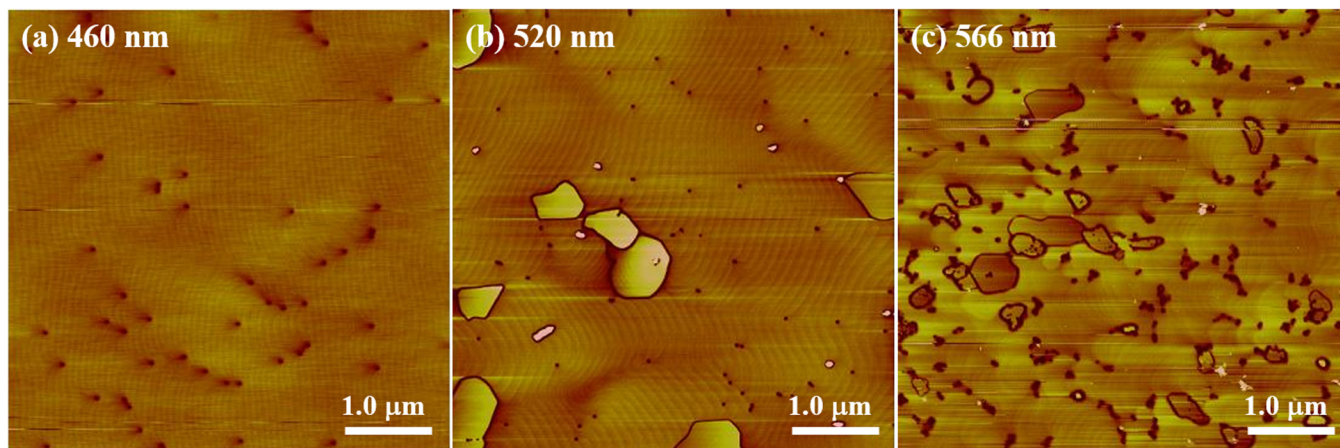


FIG. 7. AFM image of InGaN/GaN MQW samples with an emission peak wavelength of (a) 460, (b) 520, and (c) 566 nm. The height scale is 10 nm.

ABC-stacking is more stable than that for ABAB-stacking by 0.12 eV, demonstrating ABCB-stacking probably formed at the nucleation step. Here, we also account for the effect of applied strain. The ΔE monotonously rises with strain, showing that the formation of BSFs is more difficult under strain. It could have offered a technique for strain engineering to reduce the density of BSFs.

A stacking mismatch boundary (SMB) can be observed after coalescence between adjacent ABCB-stacking and ABAB-stacking regions, which should be responsible for the formation of trench defects. The results of nitrogen adatom binding on the epilayer surface are shown in Fig. 6 to confirm this. The binding energies of the N adatom on the SMB with Ga–Ga and N–N homo-elementary bonds are higher than those on a perfect surface by 0.16 and 1.04 eV, respectively. This indicates that the growth rate at the position of the SMB is lower than the surrounding area, which will result in a V-shaped groove as observed in the experimental HAADF-STEM image.

C. Experimental confirmation of the microstructure of trench defects in InGaN MQWs

Figure 7 shows the AFM images of InGaN/GaN MQW samples with peak emission wavelengths of 460, 520, and 566 nm, respectively. The increasing wavelengths are obtained by increasing the indium composition in InGaN QWs. For the sample with a peak wavelength of 460 nm [Fig. 7(a)], only V-pit defects, which are related to threading dislocations and commonly appear in InGaN QWs, are observed. For the sample with a peak wavelength of 520 nm [Fig. 7(b)], except for V-pits and indium inclusions, trench defects are observed. The trench defect density is around $3.2 \times 10^7 \text{ cm}^{-2}$, while the size varies from 0.1 to $1 \mu\text{m}$. For the sample with a peak wavelength of 566 nm [Fig. 7(c)], the density of the trench defect increases to $2.5 \times 10^8 \text{ cm}^{-2}$. The density of trench defects increases with the contents of indium, which agrees with our theoretical

prediction. References 14–16 also reported a similar tendency, implying that the substantial increase in trench defect in green InGaN/GaN MQWs is widespread.

Then, HAADF-STEM images from the $(11\bar{2}0)$ plane are examined for the sample with a peak wavelength of 520 nm. Figure 8(a) shows the HAADF-STEM images of the cross section of trench defects. The V-shaped groove is the boundary of trench

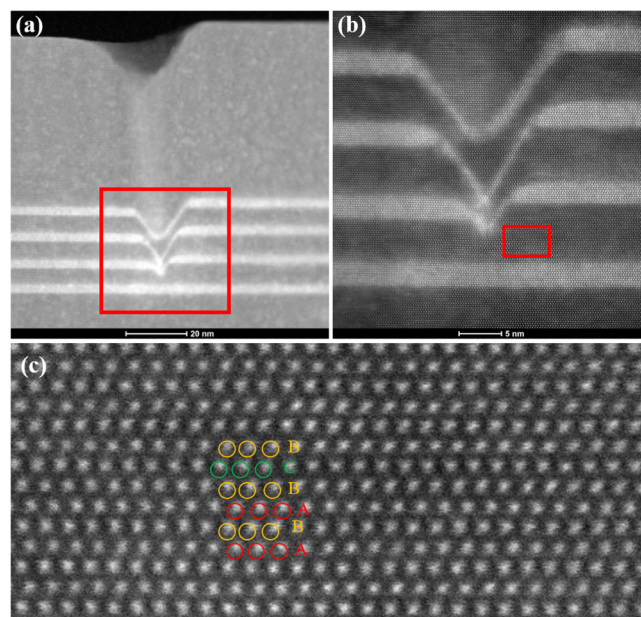


FIG. 8. HAADF-STEM images of green InGaN/GaN MQWs, (b) zoom-in of the area marked by red square in (a), and (c) zoom-in of the area marked by red square in (b).

14 March 2024 06:43:58

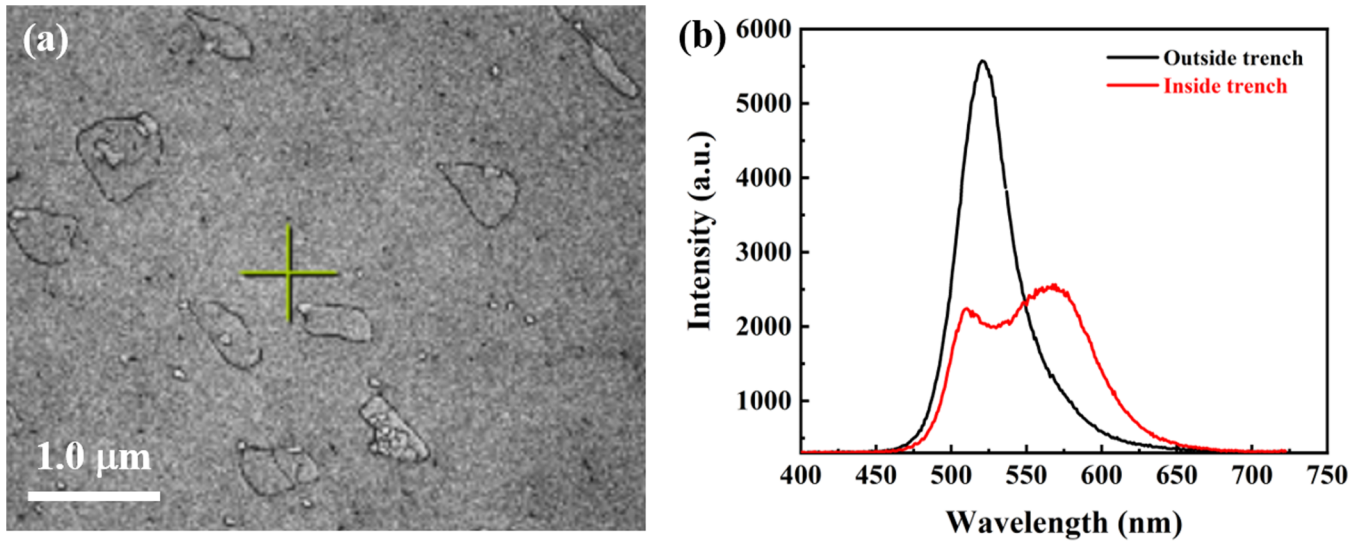


FIG. 9. (a) SEM image and (b) CL spectra inside and outside the trench defect.

defects, which is similar to the reports in the literature.⁷ Additionally, it is demonstrated that the epilayer is thinner inside the trench defects than it is outside of them. Figure 8(b) is the zoom-in view of the area marked by the red square in Fig. 8(a). It is clearly shown that the bottom of the V-shaped groove forms in the GaN QB layer. The thickness of the InGaN QW layer is thinner in the sidewall of the V-shaped groove due to the slower growth rate in the SMB, as predicted by DFT calculations. The thicknesses of InGaN QW inside and outside the trench are both 2.2 ± 0.1 nm. The thicknesses of GaN QB inside and outside the trench are 4.8 ± 0.2 and 6.0 ± 0.2 nm, respectively. Thus, the enclosed region of the trench is taller than its surrounding. The trench defect originates from the second GaN QB and broadens with the growth of subsequent MQWs. High-magnification HAADF-STEM is also performed on the area marked by the red square in Fig. 8(b) to further study the details of the trench defects, as shown in Fig. 8(c). The schematic with different colors shows the stacking sequence of atoms. It is found that inside the trench defect, parallel to the bottom of the V-shaped groove, the stacking sequence changes. The change in the stacking sequence by remarking different color atoms, from ...ABAB... to ...ABCB..., suggests that there is a II-type BSF bounded by the bottom of the V-shaped groove.

Figure 9(a) shows trench defects with a density of 3.6×10^7 cm⁻² observed by SEM, which is consistent with AFM results. Then CL measurements are performed inside and outside trench defects. Figure 9(b) shows the typical CL spectra of inside and outside trench defects, respectively. There is only one single emission peak with the emission wavelength at 521 nm outside the trench defect. In contrast, there are two emission peaks inside the trench defect. The peak wavelength is 510 nm for the left peak, while it is around 567 nm for the right peak. From HAADF-STEM images, the thickness of InGaN QW inside and outside the trench is the same, at 2.2 ± 0.1 nm, so the

difference in CL spectra should not be caused by the difference in InGaN QW thickness. These results indicate that the indium content inside the trench defect is higher than that outside the trench defect, which is consistent with previous studies.²⁴ The redshift of the region of trench defects is the combined effect of indium segregation and strain relaxation; however, the indium content in this work is much higher than that of O'Hanlon's.^{19,24} Indium segregation is more severe in InGaN with higher indium content, leading to indium clusters and low-indium regions. So, two wavelengths of 510 and 567 nm observed in the CL spectra could be mainly attributed to indium segregation. Together with the fact that the density of trench defects quickly increases for green InGaN/GaN QWs with high indium composition, which was discussed before, this led us to believe that the appearance of BSF inside trench defects is related to indium segregation. Previous studies by us and other groups showed that the density of trench defects can be greatly suppressed or eliminated by thermal annealing or the introduction of H₂ carrier gas at the InGaN/GaN interface.^{25–28}

IV. CONCLUSIONS

In conclusion, using first-principles calculations and experimental verification, we are able to identify the atomic-scale formation mechanism of trench defects in InGaN MQWs. We find that the In-rich surface forms easily due to its better thermodynamic stability, particularly with high indium content. The BSFs are more likely to nucleate on In-rich surfaces compared to Ga-rich surfaces, and the trench defects result from slower growth rate along SMBs. Our theoretical predictions are confirmed by HAADF-STEM. With increasing indium content in InGaN/GaN MQWs, especially in green and longer spectrum ranges, high-density trench defects appear. The trench defects originate from GaN QBs with a V-shaped groove boundary and BSF inside.

14 March 2024 06:43:58

ACKNOWLEDGMENTS

This work was financially supported by the National Natural Science Foundation of China (NNSFC) (Nos. 61834008, U21A20495, and 12234018), the National Science Fund for Distinguished Young Scholars (No. 61725403), National Key Research and Development Program of China (No. 2017YFE0131500), Key Research and Development Program of Jiangsu province (Nos. BE2020004 and BE2021008), and Guangdong Basic and Applied Basic Research Foundation (No. 2019B1515120091). The authors are grateful for the technical support for Nano-X from Suzhou Institute of Nano-Tech and Nano-Bionics, Chinese Academy of Sciences (SINANO).

AUTHOR DECLARATIONS

Conflict of Interest

The authors have no conflicts to disclose.

Author Contributions

Z.S. and A.T. contributed equally to this work.

Zhiming Shi: Conceptualization (lead); Data curation (lead); Investigation (equal); Methodology (lead); Software (lead); Writing – original draft (lead); Writing – review & editing (lead). **Aiqin Tian:** Conceptualization (lead); Data curation (lead); Methodology (lead); Writing – original draft (lead); Writing – review & editing (lead). **Xiaojuan Sun:** Investigation (equal); Methodology (equal); Writing – review & editing (equal). **Xuan Li:** Data curation (equal); Methodology (equal); Writing – review & editing (equal). **Hang Zang:** Data curation (equal); Methodology (equal); Writing – review & editing (equal). **Xujun Su:** Data curation (equal); Methodology (equal); Writing – review & editing (equal). **Hao Lin:** Data curation (equal); Methodology (equal); Writing – review & editing (equal). **Peng Xu:** Writing – review & editing (equal). **Hui Yang:** Writing – review & editing (equal). **Jianping Liu:** Conceptualization (lead); Funding acquisition (lead); Supervision (lead); Writing – review & editing (lead). **Dabing Li:** Conceptualization (equal); Funding acquisition (equal); Supervision (equal); Writing – review & editing (equal).

DATA AVAILABILITY

The data that support the findings of this study are available from the corresponding authors upon reasonable request.

REFERENCES

¹W. P. Risk, W. P. Risk, T. Gosnell, and A. Nurmikko, *Compact Blue-Green Lasers* (Cambridge University Press, 2003).

- ²H. Ohta, S. P. DenBaars, and S. Nakamura, *J. Opt. Soc. Am. B* **27**, B45–B49 (2010).
- ³L. Jiang, J. Liu, A. Tian, Y. Cheng, Z. Li, L. Zhang, S. Zhang, D. Li, M. Ikeda, and H. Yang, *J. Semicond.* **37**, 111001 (2016).
- ⁴A. Tian, L. Hu, L. Zhang, J. Liu, and H. Yang, *Sci. China Mater.* **63**, 1348–1363 (2020).
- ⁵A. Tian, L. Hu, X. Li, S. Wu, P. Xu, D. Wang, R. Zhou, B. Guo, F. Li, W. Zhou, D. Li, M. Ikeda, H. Yang, and J. Liu, *Sci. China Mater.* **65**, 543–546 (2022).
- ⁶S. F. Chichibu, A. Uedono, T. Onuma, B. A. Haskell, A. Chakraborty, T. Koyama, P. T. Fini, S. Keller, S. P. DenBaars, J. S. Speck, U. K. Mishra, S. Nakamura, S. Yamaguchi, S. Kamiyama, H. Amano, I. Akasaki, J. Han, and T. Sota, *Nat. Mater.* **5**, 810–816 (2006).
- ⁷F.-P. Massabuau, S.-L. Sahonta, L. Trinh-Xuan, S. Rhode, T. Puchtler, M. Kappers, C. Humphreys, and R. Oliver, *Appl. Phys. Lett.* **101**, 212107 (2012).
- ⁸S. Jain, M. Willander, J. Narayan, and R. V. Overstraeten, *J. Appl. Phys.* **87**, 965–1006 (2000).
- ⁹M. Kneissl, T.-Y. Seong, J. Han, and H. Amano, *Nat. Photonics* **13**, 233–244 (2019).
- ¹⁰M. Moram and M. Vickers, *Rep. Prog. Phys.* **72**, 036502 (2009).
- ¹¹Y. Gao, D. Sun, X. Jiang, and J. Zhao, *J. Appl. Phys.* **125**, 215705 (2019).
- ¹²H. Wang, Z. Lv, S. Zhang, B. Li, Z. Wu, and H. Jiang, *Appl. Phys. Express* **12**, 105502 (2019).
- ¹³T. Suzuki, M. Kaga, K. Naniwae, T. Kitano, K. Hirano, T. Takeuchi, S. Kamiyama, M. Iwaya, and I. Akasaki, *Jpn. J. Appl. Phys.* **52**, 08JB27 (2013).
- ¹⁴F. P. Massabuau, A. Le Fol, S. Pamberter, F. Oehler, M. Kappers, C. Humphreys, and R. Oliver, *Phys. Status Solidi A* **211**, 740–743 (2014).
- ¹⁵F.-P. Massabuau, M. J. Davies, F. Oehler, S. Pamberter, E. Thrush, M. J. Kappers, A. Kovacs, T. Williams, M. A. Hopkins, C. J. Humphreys, P. Dawson, R. E. Dunin-Borkowski, J. Etheridge, D. W. E. Allsopp, and R. A. Oliver, *Appl. Phys. Lett.* **105**, 112110 (2014).
- ¹⁶A. Vaitkevičius, J. Mickevičius, D. Dobrovolkskas, Ö. Tuna, C. Giesen, M. Heuken, and G. Tamulaitis, *J. Appl. Phys.* **115**, 213512 (2014).
- ¹⁷J. Smalc-Koziorowska, E. Grzanka, R. Czernecki, D. Schiavon, and M. Leszczyński, *Appl. Phys. Lett.* **106**, 101905 (2015).
- ¹⁸S. L. Sahonta, M. Kappers, D. Zhu, T. Puchtler, T. Zhu, S. Bennett, C. Humphreys, and R. Oliver, *Phys. Status Solidi A* **210**, 195–198 (2013).
- ¹⁹G. Kusch, E. J. Comish, K. Loeto, S. Hammersley, M. J. Kappers, P. Dawson, R. A. Oliver, and F. C.-P. Massabuau, *Nanoscale* **14**, 402–409 (2022).
- ²⁰G. Kresse and J. Furthmüller, *Comput. Mater. Sci.* **6**, 15–50 (1996).
- ²¹P. E. Blöchl, *Phys. Rev. B* **50**, 17953 (1994).
- ²²J. P. Perdew, K. Burke, and M. Ernzerhof, *Phys. Rev. Lett.* **77**, 3865 (1996).
- ²³S. Grimme, J. Antony, S. Ehrlich, and H. Krieg, *J. Chem. Phys.* **132**, 154104 (2010).
- ²⁴T. J. O’Hanlon, F. C. P. Massabuau, A. Bao, M. Kappers, and R. Oliver, *Ultramicroscopy* **231**, 113255 (2021).
- ²⁵S. Ting, J. Ramer, D. Florescu, V. Merai, B. Albert, A. Parekh, D. Lee, D. Lu, D. Christini, L. Liu, and E. A. Armour, *J. Appl. Phys.* **94**, 1461–1467 (2003).
- ²⁶F. Massabuau, M. Kappers, C. Humphreys, and R. Oliver, *Phys. Status Solidi B* **254**, 1600666 (2017).
- ²⁷A. Tian, J. Liu, L. Zhang, Z. Li, M. Ikeda, S. Zhang, D. Li, P. Wen, F. Zhang, Y. Cheng, X. Fan, and H. Yang, *Opt. Express* **25**, 415–421 (2017).
- ²⁸A. Tian, J. Liu, R. Zhou, L. Zhang, S. Huang, W. Zhou, M. Ikeda, S. Zhang, D. Li, L. Jiang, H. Lin, and H. Yang, *Appl. Phys. Express* **12**, 064007 (2019).